Article | Open Access

Energy Materials

She *et al. Energy Mater.* **2026**, *6*, 600103 **DOI:**10.20517/energymater.2026.128

pH-decoupled tin redox chemistry enables high-voltage aqueous Sn-Br batteries

Leyan She[1], Jiaxin Meng[1], Lide Li[1], Litao Liang[1], Routong Chen[1], Shiyi Tan[1], Guozhen Zhang[1], He Liu[1], Cong Guo[1], Weizhai Bao[1], Jingfa Li[1], Qian Liu[2], Feng Yu[1,*], Hongxia Wang[2,*]

Keywords:
pH-asymmetric electrolyte, bipolar membrane, tin redox chemistry, aqueous Sn-Br battery

Citation: She, L.; Meng, J.; Li, L.; Liang, L.; Chen, R.; Tan, S.; Zhang, G.; Liu, H.; Guo, C.; Bao, W.; Li, J.; Liu, Q.; Yu, F.; Wang, H. pH-decoupled tin redox chemistry enables high-voltage aqueous Sn-Br batteries. *Energy Mater.* **2026**, *6*, 600103. https://dx.doi.org/10.20517/energymater.2026.128

Received: 18 May 2026
First Decision: 9 Jun 2026
Revised: 23 Jun 2026
Accepted: 29 Jul 2026
Published: 24 Aug 2026

Academic Editor:
Bin Wang
Copy Editor:
Ping Zhang
Production Editor:
Ping Zhang

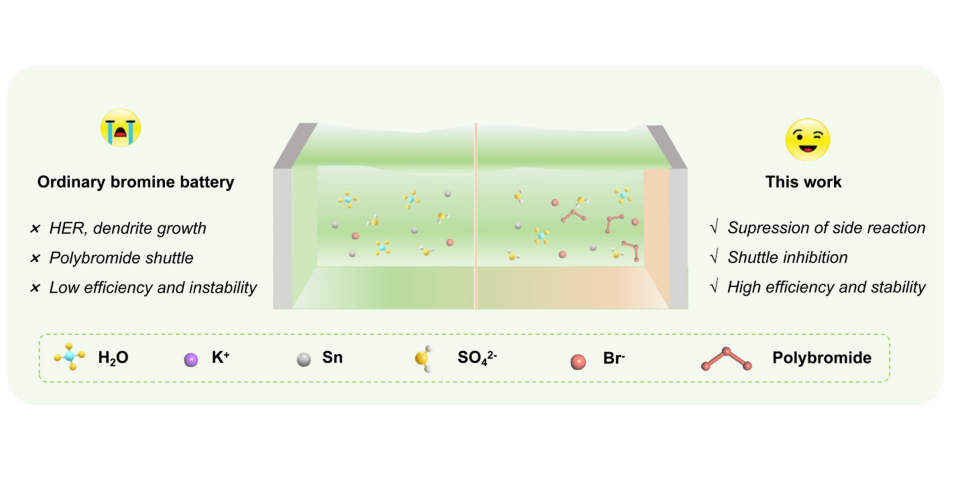

Abstract

Aqueous bromine batteries hold promise for safe and low-cost large-scale energy storage, but their practical energy density is limited by the restricted voltage of conventional single-electrolyte systems. Herein, we develop a pH-asymmetric aqueous Sn-Br battery by decoupling an acidic bromine catholyte from an alkaline Sn anolyte using a bipolar membrane. The acidic catholyte maintains reversible Br^-/Br_3^- conversion, whereas the alkaline anolyte enables low-potential Sn hydroxo-complex redox chemistry. This acid-alkaline configuration converts the pH-dependent redox asymmetry of Sn into an enlarged full-cell voltage window. A surface-regulated Sn anode is further employed to improve interfacial stability and redox reversibility, while the voltage enhancement primarily originates from pH-decoupled Sn-Br redox chemistry. Potential-alignment analysis shows that switching Sn from acidic Sn/Sn^{2+} redox to alkaline hydroxo-complex redox increases the theoretical Sn-Br potential gap from approximately 1.2 V to above 2.0 V. *In situ* Ultraviolet-Visible (UV-vis) Absorption spectroscopy confirms reversible bromine-species evolution during charge/discharge, demonstrating the compatibility of bromine redox

[1]Jiangsu Key Laboratory of New Energy Devices & Interface Science, School of Chemistry and Materials Science, Nanjing University of Information Science and Technology, Nanjing 210044, Jiangsu, China.
[2]School of Chemistry and Physics, Faculty of Science, Queensland University of Technology, Brisbane 4001, Australia.

***Correspondence to:** Dr. Feng Yu, Jiangsu Key Laboratory of New Energy Devices & Interface Science, School of Chemistry and Materials Science, Nanjing University of Information Science and Technology, Nanjing 210044, Jiangsu, China. E-mail: yufeng@nuist.edu.cn; Prof. Hongxia Wang, School of Chemistry and Physics, Faculty of Science, Queensland University of Technology, Brisbane 4001, Australia. E-mail: hx.wang@qut.edu.au

chemistry with high-voltage operation. The resulting pH-asymmetric Sn-Br full cell achieves a voltage window of up to 2.3 V, delivers a specific capacity of approximately 172.2 mAh g^{-1} at 3 A g^{-1}, and maintains 98% capacity retention over 6,000 cycles with Coulombic efficiency above 97%. This study highlights pH decoupling as a powerful strategy for designing high-voltage aqueous conversion batteries based on pH-dependent metal redox chemistry.

INTRODUCTION

Aqueous rechargeable batteries are regarded as promising candidates for large-scale energy storage because of their intrinsic safety, low cost, environmental compatibility, and high ionic conductivity[1-3]. Nevertheless, their practical energy density still lags behind that of nonaqueous batteries. This limitation originates not only from the narrow thermodynamic stability window of water, but also from the difficulty of simultaneously realizing a high-potential cathode, a stable low-potential anode, and long-term electrolyte compatibility within the same aqueous environment. Since the energy density of a full cell is determined by both capacity and voltage window, increasing the cell voltage is one of the most direct and effective strategies for improving aqueous battery performance. However, high-voltage operation in aqueous media is intrinsically challenging because lowering the anode potential often intensifies the hydrogen evolution reaction (HER), whereas raising the cathode potential may trigger oxidative electrolyte decomposition or other parasitic reactions. As a result, many aqueous battery systems have difficulty delivering high voltage, large capacity, and long cycle life at the same time. Beyond the intrinsic stability window of water, recent studies have also highlighted the roles of hydrogen-bond networks and hybrid additives in modulating electrode/electrolyte interfaces[4-6]. Developing electrode/electrolyte architectures that can enlarge the redox-potential gap while suppressing water-related side reactions is therefore a central challenge for next-generation aqueous energy storage[7].

Among various aqueous conversion chemistries, bromine-based systems are particularly attractive for high-energy storage. The Br^-/Br_2 redox couple possesses a high standard potential of 1.09 V *vs.* Standard Hydrogen Electrode (SHE) and a high theoretical capacity of 335 mAh g^{-1}, making bromine an appealing high-potential cathode chemistry[8]. In addition, bromine redox reactions are solution-mediated and generally exhibit fast reaction kinetics compared with solid-state ion insertion processes. These features suggest that bromine cathodes could provide both high capacity and high cathode potential. However, a high-potential cathode alone does not guarantee a high-voltage aqueous battery. The full-cell voltage is determined by the redox-potential difference between the cathode and anode, and the attainable voltage is further limited by HER, electrode corrosion, electrolyte decomposition, active-species crossover, and interfacial instability. Therefore, the key to constructing a high-voltage aqueous bromine battery is not only to stabilize bromine redox chemistry at the cathode, but also to identify and stabilize a sufficiently low-potential anode under compatible electrolyte conditions[9-11]. This requirement creates a fundamental compatibility challenge in conventional single-electrolyte bromine batteries. Bromine cathodes generally benefit from acidic and bromide-rich electrolytes, which help suppress bromine hydrolysis and promote reversible Br^-/Br_3^- interconversion. Such electrolyte environments are favorable for maintaining active bromine species and reducing cathode-side irreversibility. However, imposing the same acidic electrolyte on the anode severely limits the selection of low-potential metal anodes. Many metal anodes that could, in principle, provide a large voltage gap suffer from accelerated HER, chemical corrosion, low Coulombic efficiency, and structural degradation in acidic media. Consequently, the practical voltage of single-electrolyte aqueous bromine batteries is governed not only by the intrinsic potential of the bromine cathode, but also by the coupled constraints of anode redox potential, anode stability, and electrolyte pH. This pH-coupled architecture prevents each electrode from operating in its individually optimized chemical environment and thus restricts the development of high-voltage aqueous bromine batteries[12-14].

Tin metal offers a unique opportunity to address this challenge because its redox chemistry is strongly pH-dependent[15-17]. Sn is low-cost, commercially available, and capable of multi-electron redox reactions. In acidic electrolytes, Sn mainly follows the two-electron Sn/Sn^{2+} redox reaction, whose standard potential is approximately -0.14 V *vs.* SHE. Although this reaction can be used for aqueous Sn metal batteries, the relatively positive anode potential limits the full-cell voltage when paired with bromine cathodes. More importantly, acidic electrolytes accelerate HER and corrosion on Sn, competing with reversible Sn plating/stripping and leading to poor coulombic efficiency and rapid electrode degradation. In contrast, in alkaline electrolytes, Sn can participate in hydroxo-complex redox chemistry involving stannite/stannate species, leading to a substantially more negative anode potential, typically around -0.8 V to -1.0 V *vs.* SHE depending on pH and Sn-species activity[18,19]. This pronounced pH-induced potential shift suggests that pairing an alkaline Sn anode with an acidic bromine cathode could markedly increase the cell voltage[20-22]. However, such a configuration cannot be realized in a conventional single-electrolyte cell, because the electrolyte conditions required for low-potential Sn redox chemistry are incompatible with those favorable for bromine cathode reversibility. Therefore, decoupling the anodic and cathodic pH environments is essential for exploiting the voltage advantage of Sn redox chemistry in aqueous bromine batteries[23-25].

In addition to electrolyte-level pH decoupling, maintaining a stable Sn/electrolyte interface is also important for practical operation. Even when Sn is operated in an alkaline electrolyte, interfacial water reduction, local pH fluctuations, and possible active-species crossover may still trigger parasitic reactions and decrease Sn redox reversibility. Therefore, mild surface regulation of the Sn anode can be used as an auxiliary strategy to suppress hydrogen-related side reactions and improve interfacial stability during long-term cycling. In this work, Pb modification is employed only as a stabilizing interfacial layer for the Sn anode, rather than as the origin of voltage enhancement. The enlarged cell voltage is primarily derived from the pH-dependent negative shift of the Sn redox potential enabled by the acid-alkaline electrolyte configuration[26-28].

Meanwhile, the bromine cathode also requires careful regulation to maintain high reversibility during high-voltage operation[29-31]. Static aqueous bromine batteries are susceptible to bromine volatility, polybromide dissolution, shuttle-induced self-discharge, and active-species crossover[32-36]. These issues do not directly determine the thermodynamic voltage, but they strongly affect Coulombic efficiency, capacity retention, and long-term cycling stability[37,38]. Electrolyte engineering, particularly the optimization of bromide concentration, is important for regulating polybromide speciation and promoting reversible Br^-/Br_3^- conversion. At the cell level, effective ionic separation is also required to mitigate bromide and polybromide crossover toward the anode, where they can cause self-discharge and parasitic redox reactions[39-41]. Therefore, a practical high-voltage Sn-Br battery must simultaneously address three coupled requirements: accessing the low-potential alkaline Sn redox chemistry, maintaining the acidic bromine cathode environment, and suppressing cross-contamination between the two electrolytes[42-44].

Herein, we propose a pH-asymmetric aqueous Sn-Br battery based on bipolar membrane-enabled electrolyte decoupling, in which a Pb-modified Sn anode is used as a stabilized Sn anode to improve long-term reversibility[45,46]. As shown in Figure 1, the cell consists of a stabilized Sn-based anode, represented by Pb@Sn, operating in an alkaline anolyte, an acidic bromine catholyte coupled with a Br-C cathode, and a bipolar membrane that spatially separates the two electrolyte environments. This architecture primarily relies on acid-alkaline pH decoupling to convert the pH-dependent Sn redox asymmetry into an enlarged full-cell voltage, while the stabilized Sn interface helps suppress parasitic reactions and improve cycling reversibility. The Pb-modified Sn anode is prepared through a facile galvanic replacement reaction and serves as a stabilized Sn interface to improve redox reversibility during cycling. More importantly, the bipolar membrane separates the alkaline anolyte from the acidic bromine catholyte, allowing the Sn anode to access low-potential alkaline hydroxo-complex redox chemistry while maintaining an acidic, bromide-rich

Figure 1. Design principle and working mechanism of the pH-asymmetric Pb@Sn-Br aqueous battery.

environment favorable for reversible Br^-/Br_3^- conversion at the cathode. By maintaining the pH gradient, reducing direct acid-base neutralization, and mitigating active-species crossover, the bipolar membrane enables the intrinsic pH-dependent redox asymmetry of Sn to be translated into a substantially enlarged full-cell voltage. As a result, the Pb@Sn-Br full cell achieves an enlarged voltage window of up to 2.3 V, nearly twice that of the corresponding acid-only configuration. The cell delivers a high specific capacity of approximately 172.2 mAh g^{-1} at 3 A g^{-1}, maintains stable cycling over 6,000 cycles, and exhibits Coulombic efficiency above 97%. This work demonstrates that the voltage limitation imposed by conventional single-electrolyte Sn-Br architectures can be overcome by rationally decoupling electrode pH environments, and provides a design strategy for high-voltage aqueous bromine batteries based on pH-dependent Sn redox chemistry.

EXPERIMENTAL

Materials

The chemicals and materials used in this study, including zinc nitrate hexahydrate [$Zn(NO_3)_2 \cdot 6H_2O$], terephthalic acid (H_2BDC), dimethylformamide (DMF), acetylene black, polytetrafluoroethylene (PTFE), sulfuric acid (H_2SO_4), and potassium bromide (KBr), were purchased from commercial suppliers such as Aladdin, Macklin, Sinopharm Chemical Reagent, and Energy Chemical Reagent. All reagents were of analytical grade and used as received without further purification.

Preparation of Modified Tin Anode (Pb@Sn)

Based on the metal activity series, tin is more reactive than lead, enabling the displacement of lead ions from solution by metallic tin. Commercial tin foil was first ultrasonically cleaned with acetone, ethanol, and deionized water successively to remove surface impurities. The foil was then cut into 5 × 20 mm pieces and immersed in 50 mL of a 0.5 M lead acetate solution for varying durations (designated as Pure Sn, Soak 4 h, Soak 8 h, and Soak 12 h). After immersion, the samples were rinsed with deionized water and anhydrous ethanol, then dried at 60 °C under vacuum for 12 h.

Preparation of KBr solutions with different concentrations

Solutions with varying concentration ratios were prepared based on molarity (M = mol L^{-1}). All electrolyte preparations were conducted under ambient conditions. The following concentration gradients were prepared: 1 M H_2SO_4 (0 M KBr), 1 M H_2SO_4 + 0.5 M KBr, 1 M H_2SO_4 + 1 M KBr, and 1 M H_2SO_4 + 1.5 M KBr. The detailed procedure is as follows: First, 28 mL of concentrated sulfuric acid (98% by weight) was measured and added to 500 mL of deionized water under stirring to prepare a 1 M H_2SO_4 solution as the blank control. All stirring steps were performed at room temperature (25 °C) with magnetic stirring at 500 rpm for 30 min. Then, 29.75 g of KBr was added to the 1 M H_2SO_4 solution to obtain the 0.5 M KBr electrolyte. The same procedure was repeated to prepare the 1 M KBr and 1.5 M KBr solutions by adding the corresponding amounts of KBr.

Preparation of metal organic framework-5-derived porous carbon cathode material

In this study, Metal Organic Framework-5 (MOF-5)-derived porous carbon (denoted as PC) was selected as the cathode material. MOF-5 was synthesized by dissolving 18 mmol of $Zn(NO_3)_2$ and 6 mmol of terephthalic acid (H_2BDC) in 75 mL of DMF. The mixture was subjected to solvothermal reaction at 120 °C for 8 h. After the reaction, the resulting precipitate was thoroughly washed with DMF and anhydrous ethanol, followed by drying in a vacuum oven at 80 °C for 12 h. Subsequently, the as-prepared MOF-5 sample was placed in a ceramic boat and annealed under an N_2 atmosphere. The furnace temperature was increased from ambient to 930 °C at a heating rate of 3 °C·min^{-1}. After annealing, the sample was allowed to cool naturally to room temperature. The sintered PC (as the active cathode material) was mixed with PTFE and acetylene black in a weight ratio of 8:1:1. Using the clay electrode method, several disks weighing approximately 2 mg each were formed. One such disk was pressed onto a carbon rod. Finally, the electrode was dried at 80 °C for 12 h and used as the cathode. All specific capacities reported in this work are calculated based on the total mass of the active positive electrode components, which includes both the PC and the bromine species (the mass of PTFE and acetylene black is excluded). This normalization approach is intentionally more conservative than those commonly adopted in the literature, where the capacity is often normalized either solely by the mass of bromine (neglecting the carbon host's contribution, leading to artificially high values) or solely by the mass of carbon (neglecting the bromine's contribution). By accounting for both components, our reported capacity values represent a genuine and reliable assessment of the composite electrode's performance.

Assembly of the three-electrode system electrochemical cell

In this study, all experiments employing the three-electrode system were conducted using a 50 mL Luggin-type electrochemical cell. A saturated calomel electrode (SCE) served as the reference electrode, and a platinum sheet was used as the counter electrode. The active material electrode attached to a carbon rod functioned as the working electrode.

Assembly of the acid-alkaline dual-electrolyte battery

The full cell was constructed using a custom cylindrical dual-electrolyte cell. The cylindrical symmetric cell features interconnected side openings near the bottom. During assembly, the structure was secured with rubber bands, and appropriate separators were placed prior to reinforcement according to the battery design requirements. To investigate the influence of different anolyte pH values on the electrochemical performance of the battery system, the catholyte in the cylindrical cell consisted of 10 mL of 1 M H_2SO_4 + 1 M KBr solution, while the anolyte was composed of either 10 mL 1 M KOH + 0.01 M $SnSO_4$ + 0.001 M $(CH_3COO)_2Pb$. When both sides of the symmetric cell contained acidic electrolytes, a Nafion 212 membrane was used as the separator. In cases where the electrolytes on the two sides differed in pH (acidic *vs.* alkaline), a bipolar membrane (BPM) was employed as the separator. All separators were commercially obtained and used as received without pretreatment. The assembled cylindrical symmetric cell was filled with the

respective electrolytes, and the corresponding cathode and anode were inserted to ensure complete immersion in the electrolytes. The cell was then allowed to stand at room temperature for 24 h before electrochemical performance testing. All assembly steps were carried out under ambient atmospheric conditions, with no specific environmental requirements.

Materials characterizations

The structure and morphology of the as-prepared materials were systematically characterized using multiple analytical techniques. X-ray diffraction (XRD) analysis was conducted on a Smart Lab X-ray diffractometer (Rigaku, Japan) with Cu Kα radiation (λ = 1.54059 Å), scanning from 5° to 80° at a rate of 5° min^{-1}. Scanning electron microscopy (SEM) images mapping were obtained using a Zeiss Gemini SEM G300 instrument, with accelerating voltages ranging from 5 kV to 15 kV. Fourier transform infrared (FTIR) spectra were recorded on a Nicolet iS20 spectrometer (Thermo Fisher, USA) in the range of 500-2,000 cm^{-1} using KBr pellets. X-ray photoelectron spectroscopy (XPS) analysis was performed on an EscaLab 250Xi system (Thermo Fisher, USA) with a monochromatic Al Kα source, and all spectra were calibrated using the C 1s peak. Raman spectra were collected to analyze chemical bonding and crystallinity, and Ultraviolet-Visible (UV-vis) Absorption spectroscopy were measured using a TU-1810 spectrophotometer (Puxi, China) from 190 to 600 nm with a 0.1 nm interval.

Electrochemical measurements

Electrochemical performance was evaluated using various testing methods. Galvanostatic charge-discharge (GCD) tests were carried out on a BTS-4008 battery test system (Neware, China) for coin cells, while a CHI 660E/760E electrochemical workstation (CH Instruments, China) was used for three-electrode setups. Coulombic efficiency (CE) was calculated from the discharge and charge capacities during cycling. Symmetric cell tests were conducted using identical electrodes to assess cycling stability and deposition/stripping behavior. Cyclic voltammetry (CV) measurements were performed at scan rates ranging from 1 mV s^{-1} to 20 mV s^{-1} to investigate reaction kinetics and electrochemical behavior.

Auxiliary equipment

The auxiliary equipment used for sample preparation includes an ultrasonic cleaner (KH-250DE, Kunshan Hechuang, China), a tube furnace (OTF-1200X, Hefei Kejing, China), an analytical balance (ME155DU, Mettler Toledo, Shanghai, China), a tablet press (HY-12, Tianjin Tiangong, China), a magnetic stirrer (MS-06SU, USA), a blast drying oven (DHG-9030A, Shanghai Jinghong, China), a slicing machine (MSK-T10, Shenzhen Kejing, China), and a coincell crimper (MSK-110, Shenzhen Kejing, China).

RESULTS AND DISCUSSION

Surface regulation and structural characterization of Sn anode

To obtain a structurally stable Sn-based anode for pH-asymmetric Sn-Br batteries, tin foils were subjected to a mild surface-regulation treatment for different durations. Figure 2A shows the XRD patterns of Sn foils immersed in a lead acetate solution for different durations. The diffraction pattern of the Pure Sn sample matches well with that of metallic Sn (JCPDS, PDF#04-0673)[24]. For the sample treated for 4 h, no obvious new diffraction peak is observed compared with the untreated Sn foil. This result suggests that the surface-regulated layer formed at the early stage is thin and/or has a low Pb content, making it difficult to be detected by bulk-sensitive XRD analysis. When the treatment time is increased to 8 h, a weak diffraction peak assigned to metallic Pb (JCPDS, PDF#87-0663) appears near 2θ = 34°, indicating the occurrence of surface replacement/deposition8. After 12 h of treatment, the Pb-related diffraction signal becomes more pronounced, accompanied by slight changes in the main Sn diffraction peaks. The enhanced peak near 2θ = 34° suggests increased Pb-containing species on the Sn surface, while the slight variation of Sn peaks implies the possible formation of a surface Sn-Pb alloyed phase or solid-solution-like structure.

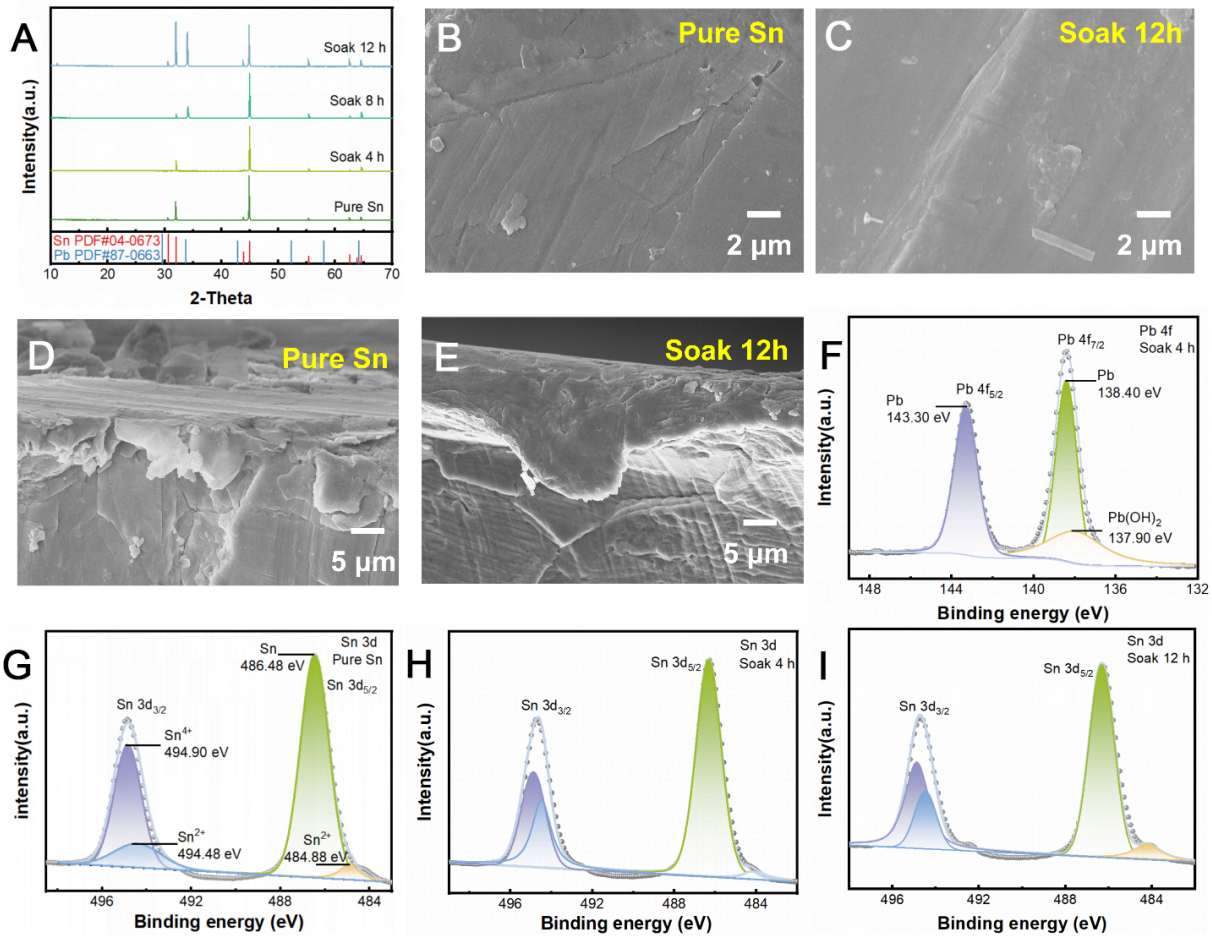

Figure 2. (A) XRD spectra of Pb@Sn negative electrode; SEM image of the surface of Pb@Sn anode: (B) Pure Sn and (C) Soak 12 h. Cross-sectional SEM images of tin sheets at different treatment times: (D) Pure Sn and (E) Soak 12 h. (F) XPS fitted curves of elemental Pb for Soak 4 h. XPS fitting curves for elemental Sn for (G) Pure Sn, (H) Soak 4 h, and (I) Soak 12 h samples. XRD: X-ray diffraction; SEM: scanning electron microscopy; XPS: X-ray photoelectron spectroscopy.

To further characterize the structural evolution of the surface-regulated Sn anode, surface and cross-sectional SEM analyses were performed before and after treatment. As shown in Figure 2B, the Pure Sn foil exhibits a relatively flat surface with slight rolling-induced folds and no obvious corrosion or deposition features. As shown in Supplementary Figure 1, after 4 h of treatment, corrugated features appear on the Sn surface, forming bright stripe-like structures with a width of approximately 0.5 μm. Slight surface etching and localized deposits are also observed, which can be attributed to the initial surface replacement reaction between Sn and Pb^{2+} species. With prolonged treatment time, the Sn surface evolves into a mud-cracked and stacked morphology, with increased lamellar features and a more continuous deposited layer, indicating the gradual growth of Pb-containing surface species. When the treatment time reaches 12 h, broad and well-defined corrugated protrusions are formed on the surface. Compared with the rough striated features observed after 4 and 8 h of treatment, the 12 h sample exhibits a relatively continuous Pb-containing surface layer on the Sn foil [Figure 2C]. Furthermore, Figure 2D-E and Supplementary Figure 2 present cross-sectional SEM images of the Sn foils treated for different durations. These observations indicate that the surface replacement process gradually constructs a compact Pb-containing outer layer on the Sn substrate, forming a surface-regulated Sn-based anode.

To further identify the surface chemical states generated by the regulation treatment, XPS analysis was performed on the Pb@Sn anode surface [Supplementary Figure 3]. The XPS results reveal the formation of a

Pb-containing surface layer, which is expected to help stabilize the Sn/electrolyte interface and improve Sn redox reversibility during cycling. Samples treated for 4, 8, and 12 h were analyzed, with untreated Sn foil used as the control. After 4 h of treatment, the Pb 4f spectrum [Figure 2F] can be deconvoluted into Pb-related components, including metallic/alloyed Pb and oxidized Pb species such as Pb-O/Pb-OH, indicating the partial reduction of Pb^{2+} and the formation of surface Pb-containing species. With extended treatment to 8 h, the evolution of the Pb 4f signal suggests strengthened Pb-Sn interaction [Supplementary Figure 4] and the possible formation of an alloyed surface component, consistent with the XRD results. The gradual formation of Pb-containing species and possible Pb-Sn alloyed components contributes to a more stable Sn surface, which can help suppress hydrogen-related parasitic reactions. This surface layer does not determine the enlarged voltage window; instead, it mainly improves the practical reversibility of the Sn anode, while the high-voltage output originates from the pH-dependent negative shift of Sn redox potential in the acid-alkaline cell configuration. The Sn 3d spectra [Figure 2G-I and Supplementary Figure 5] further reveal the coexistence of Sn^{0}, Sn^{2+}, and Sn^{4+} species, with metallic Sn remaining dominant, indicating that the surface-regulation treatment does not substantially alter the bulk Sn chemistry. Collectively, the XPS results demonstrate that the Pb-containing surface layer modifies the outer Sn interface while retaining the dominant Sn chemistry, providing an auxiliary stabilization effect for subsequent electrochemical operation.

To evaluate the interfacial stability of the surface-regulated Sn anode, Linear Sweep Voltammetry (LSV) and Tafel polarization measurements were first conducted to compare the hydrogen-related side reactions on different Sn electrodes. As shown in Figure 3A and B, the surface-regulated Sn anode shows a lower hydrogen evolution current and a more positive corrosion potential than pure Sn, suggesting reduced hydrogen-related parasitic reactions. The Tafel analysis further indicates slower hydrogen-evolution kinetics on the surface-regulated Sn electrode, which is beneficial for improving the practical stability of the Sn/electrolyte interface. It should be emphasized that the enlarged voltage is mainly derived from the pH-dependent negative shift of the Sn redox potential in the acid-alkaline configuration, while the reduced HER activity mainly contributes to improved interfacial durability and cycling reversibility.

Symmetric cell tests were further conducted to assess the cycling reversibility and interfacial robustness of the surface-regulated Sn anode under acidic stress conditions. GCD tests were first performed in 0.5 M H_2SO_4 at 5 mA mg^{-1} within -0.5-2 V as an acidic stress test [Figure 3C and D]. The pure Sn electrode exhibits severe voltage fluctuations, with charge voltages exceeding 1.5 V and discharge voltages dropping below 0 V, indicating unstable interfacial behavior and pronounced parasitic side reactions. In contrast, the surface-regulated Sn electrode treated for 4 h delivers more stable voltage profiles, and the 12 h-treated sample shows further improved cycling stability. The optical images in Figure 3C show that the untreated Sn electrode suffers from severe corrosion and structural damage after cycling, whereas the surface-regulated Sn electrode retains a more compact morphology with much less surface degradation. Under acidic testing conditions, Pb-containing surface species may partially convert into sulfate-containing components, which can contribute to the formation of a more stable outer interfacial layer. Such an interfacial layer is expected to reduce direct contact between Sn and the acidic electrolyte and lower the tendency for hydrogen-related side reactions, thereby improving interfacial stability during repeated cycling. These effects mainly support stable Sn electrode operation and should be distinguished from the pH-decoupling mechanism that determines the enlarged voltage window.

To further evaluate the influence of surface regulation and Pb-containing additives on Sn interfacial stability, symmetric cells were assembled using untreated or surface-regulated Sn electrodes in 1 M H_2SO_4, with 0.001 M $PbSO_4$ introduced as an electrolyte additive for comparison [Figure 3E]. The pure Sn symmetric cell exhibits random voltage fluctuations, indicative of unstable interfacial reactions and severe hydrogen-related side reactions. Upon introduction of the $PbSO_4$ additive, the voltage fluctuations are partially suppressed,

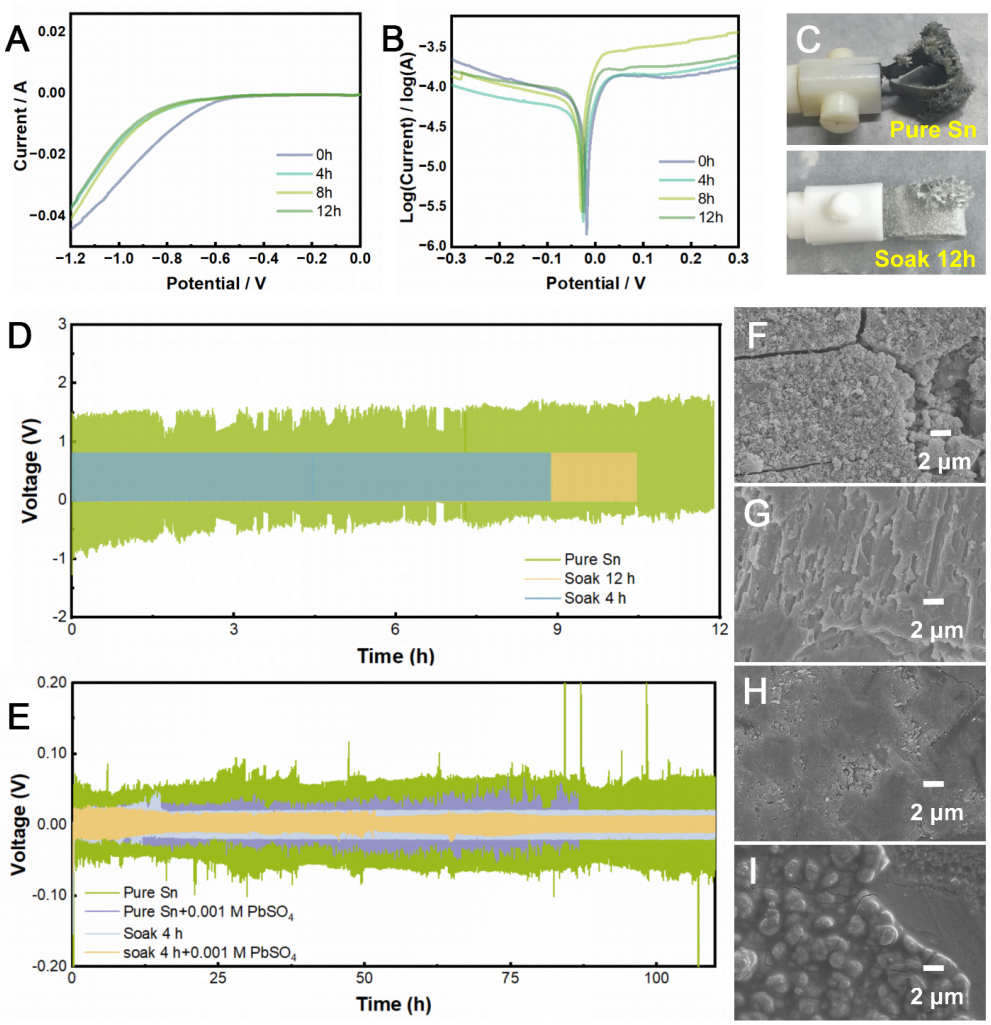

Figure 3. Electrochemical and morphological evaluation of surface-regulated Sn electrodes. (A) LSV curves and (B) Tafel plots of Sn foils treated for different durations; (C) Optical photographs and (D) voltage-time profiles of symmetric cells based on different Sn electrodes at a current density of 5 mA mg^{-1}; (E) Voltage-time profiles of Sn-based symmetric cells at 0.1 mA cm^{-2} with or without $PbSO_4$ additive; Post-cycling SEM images of (F) pure Sn, (G) pure Sn + 0.001 M $PbSO_4$, (H) the 4 h-treated Sn electrode, and (I) the 4 h-treated Sn electrode + 0.001 M $PbSO_4$. SEM: Scanning electron microscopy; LSV: linear sweep voltammetry.

suggesting that Pb-containing species can participate in interfacial regulation during cycling. The surface-regulated Sn electrode exhibits improved stability over 100 h of cycling, and the combination of the regulated Sn surface with the $PbSO_4$ additive further reduces polarization and stabilizes the voltage response. These results indicate that Pb-related surface regulation can improve the interfacial reversibility of Sn electrodes by mitigating hydrogen-related side reactions; however, the enlarged cell voltage is governed by the acid-alkaline pH decoupling discussed below.

Post-cycling SEM analysis [Figure 3F-I] was conducted to examine the morphological evolution of Sn electrodes after repeated cycling. The pure Sn electrode exhibits severe surface cracking and irregular deposits after 50 cycles, consistent with unstable interfacial reactions and structural degradation. With the $PbSO_4$ additive alone, surface pitting remains visible, indicating that electrolyte additive regulation alone provides limited surface protection. In contrast, the surface-regulated Sn electrode shows only minor surface porosity without severe degradation, suggesting improved interfacial robustness. When the $PbSO_4$ additive is combined with the surface-regulated Sn electrode, a relatively uniform granular surface layer is formed

without obvious dendritic growth, further improving interfacial uniformity. These observations show that Pb-related surface regulation improves the morphological stability of Sn during cycling, providing an auxiliary interfacial-stabilization effect for the pH-asymmetric Sn-Br full cell. It should be noted that although the 12 h-treated Sn anode exhibits a more continuous Pb-containing layer, the 4 h-treated sample provides a balanced trade-off between interfacial stability and polarization. Moreover, the thinner Pb layer in the 4 h sample minimizes any potential interference with the intrinsic Sn redox chemistry, while the shorter treatment time is more favorable for practical scalability. Therefore, the 4 h-treated Sn anode was selected for full-cell tests.

Following the evaluation of Sn anode stability, the bromide concentration in the acidic catholyte was optimized to promote efficient bromine redox chemistry. It should be noted that catholyte optimization improves bromine utilization and reaction reversibility, rather than determining the voltage window of the full cell. Acidic catholytes containing 1 M H_2SO_4 with different KBr concentrations (0, 0.5, 1.0, and 1.5 M) were evaluated.

CV tests were conducted in a three-electrode system [Figure 4A, Supplementary Figures 6 and 7]. After KBr was introduced, a distinct pair of redox peaks appeared at 0.69/0.90 V *vs.* SCE, corresponding to the Br^-/Br_3^- redox couple. The peak positions show only slight shifts with increasing scan rate, indicating favorable electrochemical reversibility. As the KBr concentration increases from 0.5 M to 1.0 M, the CV curves retain a well-defined redox couple with enhanced peak currents. However, further increasing the KBr concentration to 1.5 M leads to decreased peak currents and reduced integrated areas, suggesting less favorable Br^-/Br_3^- conversion, probably due to altered polybromide speciation and/or mass-transport limitations at high bromide concentration.

GCD measurements [Figure 4B and Supplementary Figure 8] further support this conclusion. The 0.5 M KBr catholyte delivers specific capacities of 176.3-154.2 mAh g^{-1} as the current density increases from 1 A g^{-1} to 5 A g^{-1}, with discharge plateaus located at approximately 0.7-0.9 V. When the KBr concentration is increased to 1 M, the discharge capacity is substantially improved, reaching 208.4 mAh g^{-1} at 1 A g^{-1} and retaining 204.7 mAh g^{-1} at 5 A g^{-1} under the present capacity-normalization method. In contrast, the 1.5 M KBr catholyte shows capacities comparable to those of the 0.5 M system (174.9-163.9 mAh g^{-1}), suggesting that excessive bromide does not further improve bromine utilization and may instead cause unfavorable polybromide speciation and sluggish mass transport. Detailed electrochemical data obtained at different scan rates and current densities are provided [Figure 4C and D]. Based on these results, 1 M KBr is identified as the optimal concentration, which supports efficient Br^-/Br_3^- conversion and improves bromine utilization for subsequent pH-asymmetric full-cell operation.

Voltage enhancement via pH-asymmetric design

Based on the optimized anode and catholyte identified above, a cylindrical pH-asymmetric Sn-Br full cell was assembled using sintered MOF-5-derived porous carbon as the bromine cathode host and the 4 h-treated Sn foil as the anode [Supplementary Figure 9]. The cell employed 1 M KBr + 1 M H_2SO_4 as the acidic catholyte and 1 M KOH-based alkaline solution as the anolyte.

In aqueous bromine batteries, the output voltage is fundamentally determined by the redox-potential gap between the anode and cathode, which can be rationally enlarged by independently regulating the chemical environments of the two electrodes. To clarify the origin of the voltage enhancement in the present pH-asymmetric Sn-Br system, the pH-dependent Sn redox chemistry and the corresponding electrode-potential alignment were analyzed, as shown in Figure 5A and B. The Pourbaix-type diagram in Figure 5A reveals that the dominant Sn species and their equilibrium potentials vary markedly with electrolyte pH. As the pH

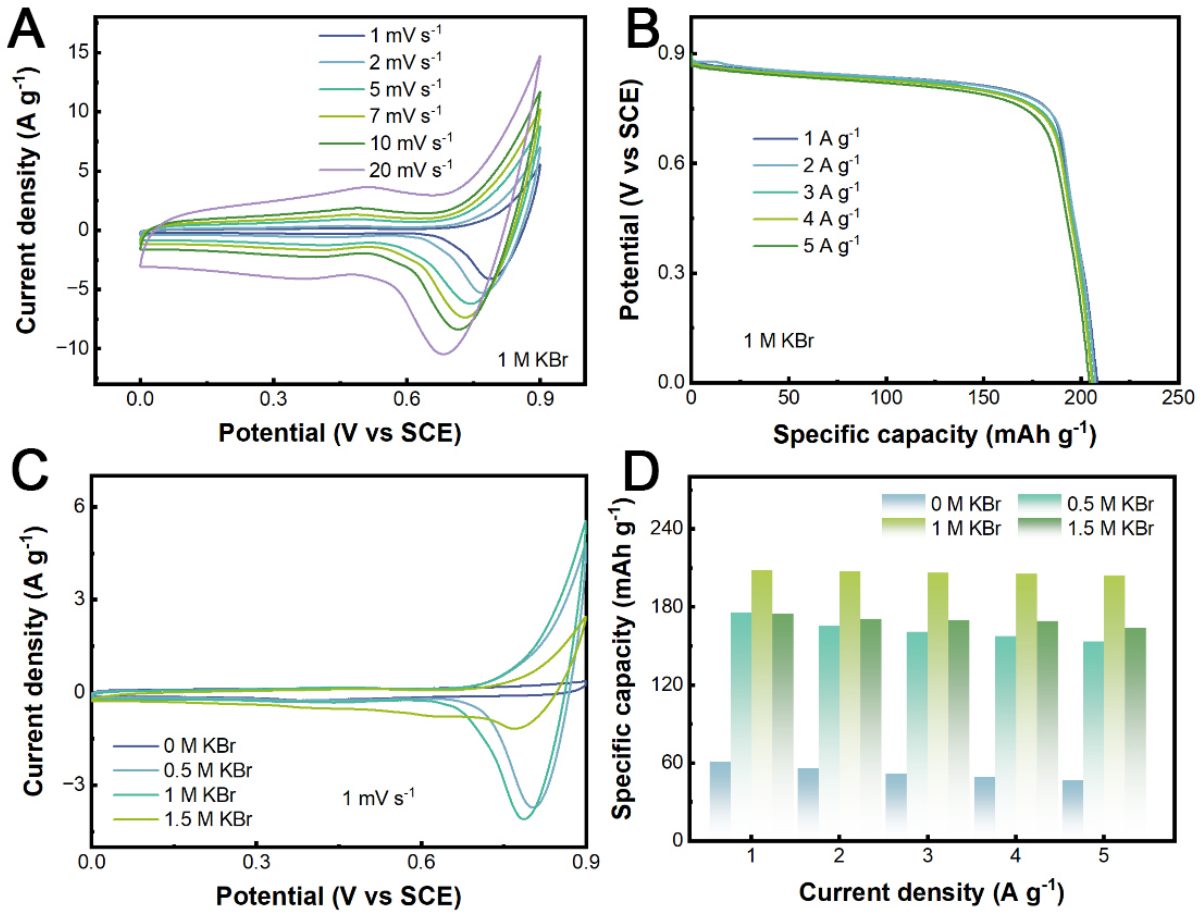

Figure 4. (A) CV curves obtained at different scan rates and (B) Discharge for 1 M KBr electrolyte in the three-electrode system. Comparison of (C) CV curves and (D) discharge specific capacity for different concentrations of KBr electrolyte. CV: Cyclic voltammetry; SCE: saturated calomel electrode.

increases from acidic to alkaline, the stable Sn species shift from Sn^{2+} to Sn hydroxo-complexes {e.g., $[Sn(OH)_3]^-$, $[Sn(OH)_6]^{2-}$}, accompanied by a substantial negative shift of the equilibrium potential by approximately 0.7-0.9 V. This trend directly explains why switching from acidic to alkaline conditions can markedly enlarge the voltage gap when paired with a bromine cathode. In acidic electrolytes, Sn mainly undergoes the Sn/Sn^{2+} redox reaction at approximately -0.14 V *vs.* SHE, giving only a limited potential gap when paired with the Br_2/Br^- cathode in acidic electrolyte at 1.09 V *vs.* SHE. In contrast, under strongly alkaline conditions, Sn participates in hydroxo-complex redox chemistry involving $Sn/[Sn(OH)_3]^-/[Sn(OH)_6]^{2-}$ conversion, and the corresponding Sn redox potential shifts substantially to more negative values, typically around -0.8 V to -1.0 V *vs.* SHE. This pH-induced negative shift is further illustrated in Figure 5B, where the acidic Sn/Sn^{2+} couple provides a theoretical cell voltage of only approximately 1.2 V against the Br_2/Br^- cathode, whereas switching the Sn anode chemistry from acidic Sn/Sn^{2+} redox to alkaline hydroxo-complex redox enlarges the anode-cathode potential separation to above 2.0 V. Therefore, the high voltage window of the present cell originates neither from altering the intrinsic Br_2/Br^- cathode potential nor from Pb modification, but from integrating an acidic high-potential bromine cathode and an alkaline low-potential Sn anode within one pH-decoupled full cell. The bipolar membrane plays a crucial role in this process by maintaining the acid-alkaline pH gradient and mitigating direct neutralization between the two electrolytes, thereby allowing the pH-dependent redox asymmetry of Sn to be translated into an expanded full-cell voltage window of up to approximately 2.3 V.

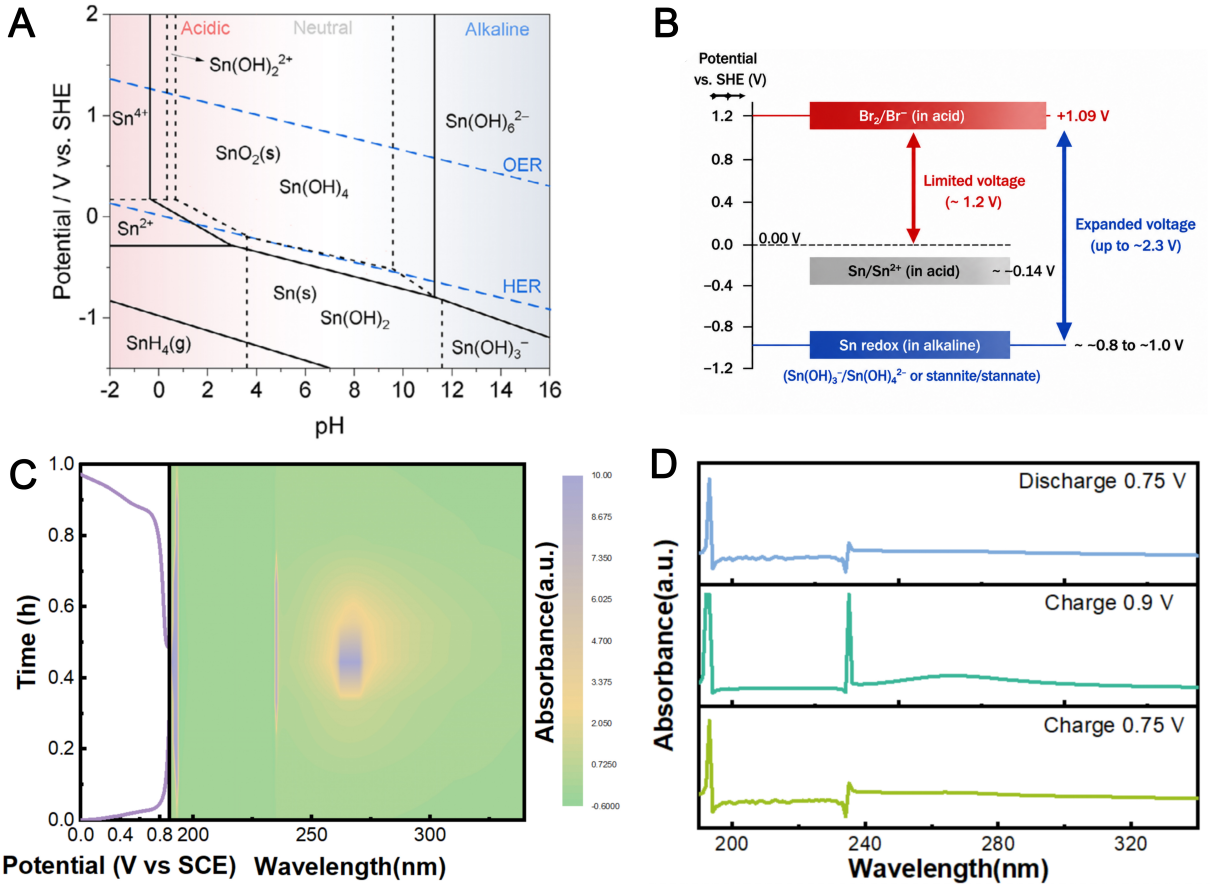

Figure 5. Voltage-enhancement mechanism and bromine redox reversibility in the pH-asymmetric Sn-Br system. (A) Pourbaix diagram of the Sn-H_2O system at 298 K, with dissolved Sn activity of 10^{-6} and p(SnH_4) = 1. Reproduced with permission from Ref[13]. Copyright © 2025, The Author(s). Advanced Materials published by Wiley-VCH GmbH; (B) Schematic illustration of the electrode-potential alignment in the acid-alkaline dual-electrolyte configuration; (C and D) *In situ* UV-Vis spectra and corresponding contour plots of bromine-species evolution during charge/discharge at a current density of 0.5 A g^{-1}. SCE: Saturated calomel electrode; SHE: standard hydrogen electrode; UV-Vis: ultraviolet-visible.

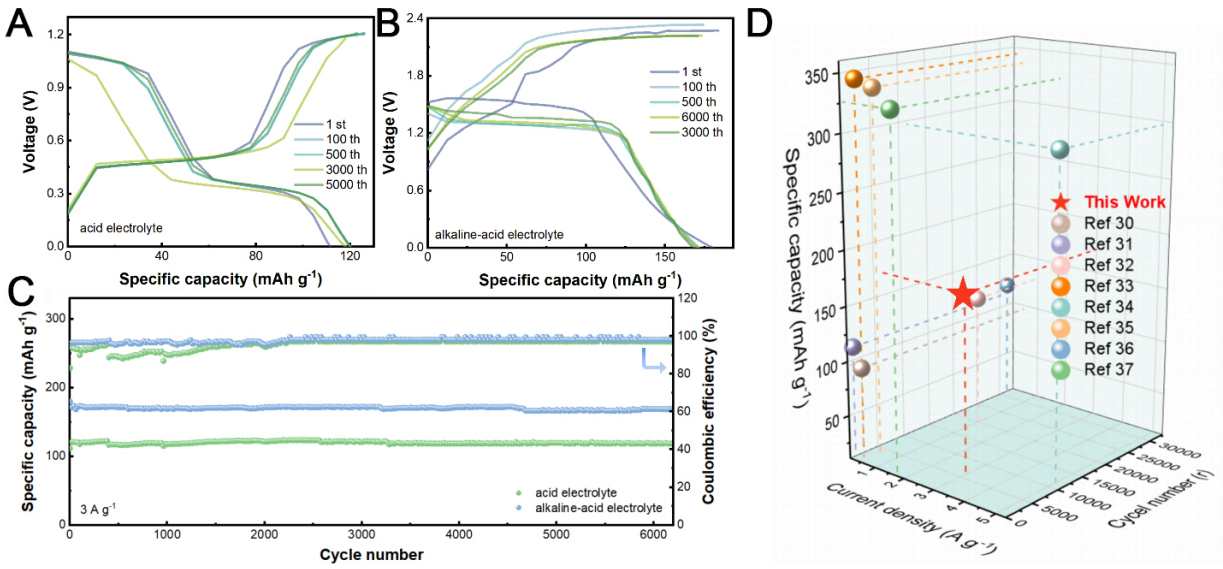

Figure 6. Electrochemical performance of acid-only and pH-asymmetric Sn-Br full cells Charge/discharge profiles of (A) the acid-only full cell and (B) the acid-alkaline pH-asymmetric full cell at a current density of 3 A g^{-1}; (C) Long-term cycling performance of the acid-only and pH-asymmetric full cells at 3 A g^{-1}; (D) Performance comparison of the pH-asymmetric Sn-Br full cell with previously reported bromine-based batteries (detailed electrolyte compositions, electrode materials, and test conditions are provided in Table 1).

Table 1. Summary of key parameters of the bromine-based battery systems cited for performance comparison

System	Anode	Electrolyte	Cathode	Voltage/V	Ref
Zn-Br_2 static battery	Zn foil	2 M $ZnBr_2$ + 0.4 M M6 (organic bromide) + 0.1 M $ZnSO_4$	Carbon felt with M6 bromide	1.8	[29]
Zn-Br_2 metal-free battery	Tp-DANT-COF	2 M $Zn(CF_3SO_3)_2$ aqueous	AC-KBr (activated carbon with KBr)	1.2	[30]
MoO_{3-x}@TiO_2-Br_2 membrane-less battery	MoO_{3-x}@TiO_2 (oxygen-deficient MoO_3 with TiO_2 coating)	1 M $AlCl_3$ + 50 mM KBr	Carbon nanotubes (CNTs)	1.5	[31]
Zn-Br_2 battery with single-atom catalyst	Zn foil	2 M $ZnSO_4$	FeSAC-CMK (Fe single-atom catalyst on mesoporous carbon) with Br_2	1.8	[32]
Zn-Br_2 static battery	Zn foil	HDES ($ZnBr_2$:$ZnCl_2$:EG = 1:2:9, 30 wt% H_2O, 0.1 M TBABr)	Activated carbon	1.8	[33]
Zn-I/Br hybrid battery	Zn foil	2 M $ZnSO_4$ (halide-free)	$TmdpPb_2[IBr]_6$ (low-dimensional perovskite)	1.74	[34]
Zn-Br_2 static battery	Zn foil	0.5 M $ZnBr_2$ + 0.25 M TPABr	PAM@$TPABr_3$ (quasi-solid, PAM-encapsulated)	1.6	[35]
Mg-Br_2 battery	Mg metal	0.5 ICD [$Mg(TFSI)_2$ + $2MgCl_2$ in DME]	SN-Mg-Br (succinimide-Mg-Br complex)	2.7	[36]

DME: Ethylene glycol dimethyl ether; Tp-DANT-COF: 1,3,5-triformylphosphorolucinol-2,7-diaminobenzol[1mn][3,8]phenanthrolin-1,3,6,8-tetrane covalent organic framework. Tp-DANT-COF was synthesized from 2,7-Diaminobenzol[1mn][3,8] phenanthrolin-1,3,6,8-tetrane (DANT), and 1,3,5-triformylphosphorolucinol (Tp)

To verify that the bromine cathode can provide reversible Br^-/Br_3^- conversion compatible with the pH-asymmetric full-cell design, *in situ* UV-Vis spectroscopy was employed. The test was conducted in a three-electrode system using 1 M KBr as a model bromide electrolyte at a current density of 0.5 A g^{-1} within a potential window of 0-0.9 V. The *in situ* UV-Vis spectra and corresponding contour plots recorded during the charge/discharge process are shown in Figure 5C and D. During charging, the characteristic absorption band at approximately 280 nm gradually appears, indicating the formation of polybromide species, and this band nearly disappears upon discharge, suggesting reversible bromine-species conversion. The absorption signals at 191 and 238 nm can be associated with bromine-related intermediate species, reflecting the dynamic evolution of bromine speciation during cycling. Upon charging, Br^- is oxidized to bromine-related intermediate species, which subsequently participate in polybromide formation. As charging proceeds, the increasing absorption intensity indicates the continuous accumulation of oxidized bromine species. These oxidized bromine species can associate with Br^- to form polybromide species such as Br_3^-/Br_n^-, as evidenced by the absorption band near 280 nm. This observation indicates that polybromide species are the main detectable oxidized products under the present testing conditions. During discharge, the reverse reduction process occurs, in which Br_3^-/Br_n^- species are reduced back to Br^- through the coupled $Br_2/Br^-/Br_3^-$ equilibrium. Since irreversible bromine accumulation or parasitic reactions would compromise Coulombic efficiency and cycling stability in high-voltage full cells, verifying the reversibility of bromine speciation is essential. The disappearance of the 280 nm absorption band upon discharge indicates that the accumulated polybromide species can be efficiently converted back to Br^-, demonstrating the high reversibility of bromine redox chemistry under the tested cathodic conditions. The contour plot further supports the reversible interconversion of the Br^-/Br_3^- redox couple throughout the charge/discharge process. These results indicate that, under the optimized bromide chemistry, the bromine cathode is compatible with the pH-asymmetric voltage-enhancement strategy and can maintain reversible redox behavior during operation.

Electrochemical performance of pH-asymmetric Pb@Sn-Br batteries

Based on the optimized Sn anode and acidic bromine catholyte described above, full cells with different electrolyte configurations were assembled to evaluate the effect of pH-asymmetric design on electrochemical performance. In summary, the pH-asymmetric Sn-Br battery operates as follows: during charging, Br^- in the

acidic catholyte is oxidized to Br_3^- (via a Br_2 intermediate) at the cathode, while Sn-containing species {$[Sn(OH)_3]^-$} in the alkaline anolyte are reduced to Sn metal at the anode. During discharge, the reverse reactions occur: Br_3^- is reduced back to Br^- at the cathode, and Sn metal is oxidized to $[Sn(OH)_3]^-$ at the anode. The bipolar membrane effectively separates the two electrolytes, preventing neutralization and cross-contamination, thereby enabling a stable cell voltage of ~2.3 V. As shown in Supplementary Figure 10A and B, the CV curves exhibit a distinct pair of redox peaks, which is consistent with the charge-discharge plateaus observed in the corresponding GCD profiles. These peaks can be assigned to the reversible Br^-/Br_3^- redox couple in the acidic bromine catholyte. With increasing scan rate, both the anodic and cathodic peak currents increase gradually, indicating accelerated bromine redox kinetics at higher sweep rates. The calculated b values derived from the relationship $i = av^b$ are 0.486 and 0.596 for Peak 1 and Peak 2, respectively. These values, close to 0.5, suggest that the Br^-/Br_3^- redox reaction is mainly diffusion-dominated with a minor surface-controlled contribution. Such diffusion-dominated kinetics are consistent with the solution-mediated conversion behavior of bromine species, where mass transport and polybromide speciation play important roles in the overall reaction process.

Figure 6A displays the charge-discharge profiles of the acid-only Sn-Br full cell at a current density of 3 A g^{-1}. Two discharge plateaus are observed, which can be associated with the stepwise conversion of bromine species through the coupled $Br^-/Br_2/Br_3^-$ equilibrium. In contrast, Figure 6B shows the charge-discharge profiles of the acid-alkaline pH-asymmetric full cell under the same current density. Notably, the voltage window reaches 2.3 V, nearly twice that of the acid-only system, which operates at approximately 1.2 V. Moreover, the pH-asymmetric cell exhibits an elevated voltage plateau, indicating that the same bromine cathode reaction is coupled with a much lower-potential alkaline Sn anode, thereby shifting the full-cell output to a higher voltage region. The charge-discharge curves show only limited polarization growth upon cycling, suggesting improved electrochemical stability and reversibility.

Figure 6C compares the long-term cycling performance of the acid-only and pH-asymmetric full cells at 3 A g^{-1}. The acid-only full cell delivers a specific discharge capacity of approximately 121 mAh g^{-1} with a Coulombic efficiency of around 96%; after 6,000 cycles, the capacity remains at 118.4 mAh g^{-1}, corresponding to a retention of 97%. The gradual increase in CE during the first 2,000 cycles is likely due to the progressive stabilization of the electrode/electrolyte interface [e.g., formation of a more uniform Solid Electrolyte Interphase (SEI)-like layer on the Sn anode] and the gradual establishment of equilibrium among polybromide species ($Br^-/Br_2/Br_3^-$), which collectively reduce parasitic side reactions such as bromine crossover or hydrogen evolution. In the pH-asymmetric full cell, the BPM maintains the acid-alkaline electrolyte separation and mitigates bromide/polybromide crossover, enabling stable coupling between the acidic bromine cathode and alkaline Sn anode. As a result, the cell delivers a much higher specific discharge capacity of approximately 172.2 mAh g^{-1} at 3 A g^{-1}, representing a substantial increase of approximately 42% compared to the acid-only system, with a Coulombic efficiency exceeding 97%. After 6,000 cycles, the capacity remains above 169.5 mAh g^{-1}, corresponding to a capacity retention of 98%. These results demonstrate that the pH-asymmetric design effectively expands the voltage window while improving capacity retention and cycling stability, establishing the acid-alkaline Sn-Br full cell as a promising high-voltage aqueous energy-storage system [Figure 6D].

CONCLUSION

In this work, we developed a pH-asymmetric aqueous Sn-Br battery by coupling an alkaline Sn anode with an acidic bromine cathode through bipolar-membrane-enabled electrolyte decoupling. This architecture allows the Sn anode to access low-potential alkaline redox chemistry while preserving the high-potential

Br^-/Br_3^- redox reaction in acidic catholyte, thereby expanding the full-cell voltage window to 2.3 V. A surface-regulated Sn anode was employed to improve interfacial stability and redox reversibility during cycling. The Pb-containing surface layer serves mainly as an auxiliary stabilization layer that mitigates hydrogen-related side reactions and surface degradation, rather than as the origin of voltage enhancement. As a result, the pH-asymmetric Sn-Br full cell delivers a specific capacity of approximately 172.2 mAh g^{-1} at 3 A g^{-1}, retains 98% of its capacity after 6,000 cycles, and maintains a Coulombic efficiency above 97%. These results demonstrate that the voltage limitation of conventional single-electrolyte Sn-Br batteries can be effectively addressed by rationally decoupling electrode pH environments. More importantly, this work highlights pH-dependent metal redox chemistry as a powerful design principle for high-voltage aqueous conversion batteries. It is worth noting that the Pb content used in this work is relatively small. It exists both as a thin surface modification layer on the Sn anode and as a soluble Pb salt [0.001 M $(CH_3COO)_2Pb$] additive in the anolyte. These Pb species work synergistically to enhance interfacial stability and improve cycling reversibility. Nevertheless, to further improve environmental friendliness, future efforts should explore Pb-minimized or completely Pb-free interfacial regulation strategies, such as using Bi, In, or Sn-based alloys. The challenge lies in achieving comparable hydrogen suppression and morphological stability without compromising redox reversibility. It should be noted that no noble metal catalysts were used in this work; the bromine cathode relies solely on porous carbon. The use of noble metal catalysts (e.g., Pt, Ru) could potentially further enhance the reaction kinetics of bromineredox, which may be explored in future studies for higher rate capability. Future efforts may focus on Pb-minimized or Pb-free interfacial regulation, lower-resistance membrane design, long-term pH management,and scalable cell engineering for practical aqueous energy-storage applications.

DECLARATIONS

Authors' contributions

Conceptualization, methodology, investigation, writing - original draft: She, L.
Conceptualization, methodology: Meng, J.; Li, L.
Investigation, validation, resources: Liang, L.; Chen, R.; Tan, S.; Zhang, G.; Liu, H.; Guo, C.;
Writing - review & editing: Bao, W.; Li, J.; Liu, Q.; Wang, H.
Supervision, conceptualization, funding acquisition, project administration, writing - review & editing: Yu, F.

Availability of data and materials

The original contributions presented in this study are included in the article/Supplementary Materials. Further inquiries can be directed to the corresponding authors.

AI and AI-assisted tools statement

During the preparation of this manuscript, the AI tool DeepSeek (version 3, released on 2024-12-26) was used solely for language polishing. The AI-assisted tool GPT (version GPT Image 2, released 2026-04-21) was used for the preparation of Figure 1. These tools did not influence the study design, data collection, analysis, interpretation, or the scientific content of the work. All authors take full responsibility for the accuracy, integrity, and final content of the manuscript.

Financial support and sponsorship

This work was supported by the Natural Science Research of Jiangsu Higher Education Institutions of China (24KJB480012).

Conflicts of interest

All authors declared that there are no conflicts of interest.

Ethical approval and consent to participate

Not applicable.

Consent for publication

Not applicable.

Supplementary Materials

Supplementary Materials

REFERENCES

1. Zhang, H.; Xu, D.; Yang, F.; et al. A high-capacity Sn metal anode for aqueous acidic batteries. *Joule* **2023**, *7*, 971-85. DOI
2. Nigatu, T. A.; Bezabh, H. K.; Jiang, S.; et al. An anode-free aqueous hybrid batteries enabled by in-situ Cu/Sn/Zn alloy formation on pure Cu substrate. *Electrochim. Acta.* **2023**, *443*, 141883. DOI
3. Peng, Z.; Bannov, A. G.; Li, S.; et al. Coupling uniform pore size and multi-chemisorption sites: hierarchically ordered porous carbon for ultra-fast and large zinc ion storage. *Adv. Funct. Mater.* **2023**, *33*, 2303205. DOI
4. Yin, J.; Wu, Z.; Zhang, S.; Liu, X.; Liu, Y.; Tian, H. A review of the water dilemma and hydrogen-bond chemistry for aqueous zinc-ion batteries. *Energy. Environ. Sci.* **2025**, *18*, 10263-85. DOI
5. Xie, Y.; Dou, Q.; Li, G.; Chen, Y.; Yan, X. Regulating the solvation environment of hybrid electrolytes towards high-temperature zinc-ion storage. *Energy. Mater.* **2025**, *5*, 500025. DOI
6. Xue, T.; Mu, Y.; Wei, X.; et al. From fundamentals to practice: electrolyte strategies for zinc-ion batteries in extreme temperature. *Carbon. Neutral.* **2025**, *4*, e183. DOI
7. Chen, Q.; Yang, X.; Wang, C.; et al. Tailored separators for diverse batteries: design, modification, and prospects. *Energy. Z.* **2026**, *2*, 200005. DOI
8. Zhu, X.; Zhang, W.; Peng, Z.; et al. Zinc-tin binary alloy interphase for zinc metal batteries. *Chem. Eng. J.* **2024**, *499*, 156521. DOI
9. Chang, S.; Hou, W.; Del Valle-Perez, A.; et al. A low-acidity chloride electrolyte enables exceptional reversibility and stability in aqueous tin metal batteries. *Angew. Chem. Int. Ed.* **2025**, *64*, e202414346. DOI
10. Zhou, W.; Ding, S.; Zhao, D.; Chao, D. An energetic Sn metal aqueous battery. *Joule* **2023**, *7*, 1104-7. DOI
11. Tao, F.; Liu, Y.; Ren, X.; et al. Different surface modification methods and coating materials of zinc metal anode. *J. Energy. Chem.* **2022**, *66*, 397-412. DOI
12. Ruan, P.; Chen, X.; Qin, L.; et al. Achieving highly proton-resistant Zn-Pb anode through low hydrogen affinity and strong bonding for long-life electrolytic Zn//MnO_2 battery. *Adv. Mater.* **2023**, *35*, e2300577. DOI
13. Zhang, H.; Liu, D. J.; Xu, K.; Meng, Y. S. Challenges and opportunities for rechargeable aqueous Sn metal batteries. *Adv. Mater.* **2025**, *37*, e2417757. DOI PubMed PMC
14. Zhang, H.; Yu, Y.; Xu, D.; et al. Electrodepositing textured Sn film as a highly reversible anode for aqueous batteries. *J. Am. Chem. Soc.* **2025**, *147*, 19829-40. DOI
15. Du, X.; Chang, S.; Bristi, S. T.; et al. Rational design of moderately concentrated electrolytes to consolidate the electrode-electrolyte compatibility for ultrahigh-efficiency and harsh-condition-tolerant aqueous tin metal batteries. *Adv. Funct. Mater.* **2026**, *36*, e75197. DOI
16. Lan, X.; Zhang, Z.; Liao, G.; et al. Recent advances in metallic tin anodes: an emerging field of rechargeable aqueous batteries. *ACS. Appl. Mater. Interfaces.* **2025**, *17*, 24763-77. DOI
17. Shao, Y.; Jin, Z.; Li, J.; Meng, Y.; Huang, X. Evaluation of the electrochemical and expansion performances of the Sn-Si/graphite composite electrode for the industrial use. *Energy. Mater.* **2022**, *2*, 200004. DOI
18. Zhou, W.; Song, M.; Liang, P.; et al. High-energy Sn-Ni and Sn-air aqueous batteries via stannite-ion electrochemistry. *J. Am. Chem. Soc.* **2023**, *145*, 10880-9. DOI
19. Zhang, Y.; Zhang, D.; Zhou, Q.; et al. Interfacial engineering of MXene-based heterogeneous membranes with enhanced ion selectivity in vanadium redox flow battery. *Adv. Funct. Mater.* **2026**, *36*, e10597. DOI
20. Zeng, Y.; Yang, Z.; Lu, F.; Xie, Y. A novel tin-bromine redox flow battery for large-scale energy storage. *Appl. Energy.* **2019**, *255*, 113756. DOI
21. Kumar, R. S.; Tamilarasi, S.; Stephan, A. M.; Kim, A. R.; Yoo, D. J. CrS doped MOF-derived carbon implanted CoNi particles as exceedingly effectual oxygen electrocatalysts in sustainable zinc-air batteries. *Small. Methods.* **2025**, *9*, e2401515. DOI PubMed
22. Dong, Y.; Wang, R.; Yu, Y. Research progress on high-energy rechargeable Sn-based batteries. *Carbon. Energy.* **2026**, *8*, e70091. DOI
23. Xiao, T.; Liu, L.; Liu, H.; et al. Highly rechargeable aqueous Sn-metal-based hybrid-ion batteries. *Joule* **2025**, *9*, 101820. DOI
24. Yu, Z.; Wang, Q.; Li, Y.; et al. Highly reversible tin redox chemistry for stable anode-free acidic proton battery. *Joule* **2024**, *8*, 1063-79. DOI

25. Wang, Y.; Wang, N.; Wu, Z.; et al. Nanofullerene regulated electric field to achieve stable Sn metal anode for aqueous Sn batteries. *Rare. Metals.* **2025**, *44*, 3869-80. DOI
26. Perry, M. L. Decoupled architecture enables pH decoupling. *Nat. Energy.* **2024**, *9*, 367-8. DOI
27. Zhu, Y. H.; Cui, Y. F.; Xie, Z. L.; Zhuang, Z. B.; Huang, G.; Zhang, X. B. Decoupled aqueous batteries using pH-decoupling electrolytes. *Nat. Rev. Chem.* **2022**, *6*, 505-17. DOI PubMed
28. Xi, D.; Alfaraidi, A. M.; Gao, J.; et al. Mild pH-decoupling aqueous flow battery with practical pH recovery. *Nat. Energy.* **2024**, *9*, 479-90. DOI
29. Jin, J.; Liu, C.; Lei, C.; et al. Efficient aqueous static zinc-bromine batteries enabled by hydrophobic organic bromide design. *Small. Methods.* **2025**, *9*, e01045. DOI
30. Zhang, R.; Xu, H.; Luo, D.; Wang, J.; Dou, H.; Zhang, X. Modulating metal-free Zn-bromine batteries with covalent organic framework anode. *Energy. Storage. Mater.* **2024**, *67*, 103294. DOI
31. Huang, W.; Wang, H.; Yuan, B.; Ouyang, L.; Yang, L.; Zhu, M. Membrane-less MoO_3-@TiO_2-bromine battery with excellent rate capability and cyclic stability. *J. Energy. Chem.* **2024**, *93*, 316-21. DOI
32. Chen, S.; Peng, C.; Zhu, D.; Zhi, C. Bifunctionally electrocatalytic bromine redox reaction by single-atom catalysts for high-performance zinc batteries. *Adv. Mater.* **2024**, *36*, e2409810. DOI
33. Lim, Y.; Lee, G.; Kim, J. H.; Seo, J. K.; Yoo, S. J. Tetrabutylammonium bromide incorporated hydrated deep eutectic solvents: Simultaneously addressing anode stability and cathode efficiency in zinc-bromine batteries. *Energy. Storage. Mater.* **2024**, *68*, 103331. DOI
34. Wang, S.; Wang, Y.; Wei, Z.; et al. Halide exchange in perovskites enables bromine/iodine hybrid cathodes for highly durable zinc ion batteries. *Adv. Mater.* **2024**, *36*, e2401924. DOI
35. Zheng, X.; Wu, S.; Luo, R.; et al. An inter-locking quasi-solid cathode for zinc-bromine batteries with stable 32000 cycles. *Adv. Mater.* **2026**, *38*, e17292. DOI
36. Guo, L.; Chen, A.; Wang, A.; Hu, Z.; Zhang, H.; Luo, J. Rechargeable Mg-Br_2 battery with ultrafast bromine chemistry. *J. Am. Chem. Soc.* **2024**, *146*, 26855-62. DOI
37. Meng, J.; Zhang, G.; Pang, L.; et al. Zinc-bromine batteries revisited: unlocking liquid-phase redox chemistry for next-generation energy storage. *Energy. Environ. Sci.* **2025**, *18*, 9031-53. DOI
38. Liu, Y.; Meng, J.; Yu, F.; et al. Synergistic electrolyte design for high-performance static zinc-bromine batteries. *ACS. Energy. Lett.* **2025**, *10*, 5809-24. DOI
39. Kim, S. I.; Shin, K.; Kang, H.; Han, S. H.; Kim, H. T.; Chung, T. D. Asymmetric mass transport in polybromide ionic liquids and its impact on dual-plating zinc bromine batteries. *Adv. Sci.* **2026**, *13*, e22078. DOI
40. Zhao, X.; Zhu, Y.; Chen, Q.; Ma, R.; Hao, J.; Qiao, S. Z. Highly reversible aqueous anode-free cadmium-bromine batteries. *Angew. Chem. Int. Ed.* **2026**, *65*, e1396057. DOI
41. Ballas, E.; Leifer, N.; Ohayon, A.; et al. Extending the life-time of Zn-Br_2 batteries by targeted local confinement of bromine complexes. *Mater. Today.* **2026**, *96*, 103298. DOI
42. Liu, B.; Wang, S.; Wang, Z.; Lei, H.; Chen, Z.; Mai, W. Novel 3D nanoporous Zn-Cu alloy as long-life anode toward high-voltage double electrolyte aqueous zinc-ion batteries. *Small* **2020**, *16*, e2001323. DOI
43. Hu, Y.; Min, Z.; Zhu, G.; et al. Predeposited lead nucleation sites enable a highly reversible zinc electrode for stable zinc-bromine flow batteries. *Nat. Commun.* **2025**, *16*, 3255. DOI PubMed PMC
44. Katiyar, S.; Chang, S.; Ullah, I.; et al. Unlocking the potential of cadmium plating chemistry for low-polarization, long-cycling, and ultrahigh-efficiency aqueous metal batteries. *Energy. Environ. Sci.* **2024**, *17*, 4770-9. DOI
45. Wu, F.; Yang, L.; Zhou, Q.; et al. Decoupling electrode environments with a pH-asymmetric biphase electrolyte for high-voltage aqueous rocking-chair batteries. *ACS. Appl. Mater. Interfaces.* **2025**, *17*, 69489-501. DOI
46. Toh, W. L.; Chu, A. T.; Surendranath, Y. Separation of polymeric charge enables efficient bipolar membrane operation. *ACS. Energy. Lett.* **2024**, *9*, 1423-30. DOI